MICROWAVE ATOM CHIP FOR SPIN-SPECIFIC ATOM INTERFEROMETRY

William Miyahira and Seth Aubin (advisor)
Department of Physics, William & Mary, Williamsburg. VA 23185

Integration of ultracold atomic quantum sensors could yield enhanced measurement sensitivity for future NASA missions. We present research on the development of a broadband microwave atom chip for spin-specific rf and microwave AC Zeeman (ACZ) trapping. These chips can be used for trapped atom interferometric sensing of inertial and gravitational forces and allow for integration into the field given their low SWaP-C requirements. Our chip design uses parallel microstrip transmission lines to produce the transverse trapping potentials for ultracold atoms. Axial confinement and translation can be achieved using a microwave lattice based on either the ACZ or AC Stark effect. For broadband transmission of rf and microwave signals onto the atom chip we have designed a tapered microstrip wedge interface, for which we present simulation and prototype results. We also present progress on the development of the physical microwave atom chip, including characterization of the atom chip dielectric substrate and diamond turned copper surfaces for deposition. Preliminary experimental results showing qualitative evidence of potential roughness suppression in the ACZ trap is also shown.

I. INTRODUCTION

Since the first experimental realization of a Bose-Einstein condensate (BEC) in the mid-1990's[1], ultracold atoms have been used to transform the world of precision measurement. By harnessing the wave-like quantum nature of the atoms one can make an atom interferometer (AI) that is extremely sensitive to energy gradients (for example gravity) and as inertial sensors for measuring rotations and accelerations. As an example, a 10-meter tall "drop tower" AI[2] is able to measure the acceleration due to gravity to a precision of $\Delta g/g = 3{\times}10^{-11}$.

Using compact atom chip devices[3] give the ability to greatly reduce the SWAP-C requirements of the experiment and allow for the application of ultracold atom based quantum sensors in the field. These are cm-scale sized devices featuring microfabricated wires able to produce complex electromagnetic fields for trapping and manipulating ultracold atoms.

Putting ultracold atoms in space opens up additional opportunities for scientific exploration and improved precision. Currently, the Cold Atom Laboratory (CAL) aboard the International Space Station (ISS) is able to produce single- and dual-species BECs[4,5] and has been able to study novel bubble geometries[6] and perform atom interferometry experiments[7] in micro-gravity environments. Future improvements to this system in collaboration with the German Aerospace Center (DLR) will see the Bose-Einstein Condensate and Cold Atom Laboratory (BECCAL, to be launched in 2025)[8] and third generation "Quantum Explorerer"[9] to push towards having state of the art Earth-based cold atom facilities in space for enhanced quantum sensing applications and experiments.

Space-based ultracold atom quantum sensors could be used for improving resolution and precision of the GRACE-FO[10] mission in tracking planetary mass distributions (for example water) to enhance our understanding of climate change and impact agriculture and weather predictions[11]. There are also applications of these sensors for improved inertial navigation[12,13] in GPS-denied environments. On a rover, AI quantum sensors can be used to explore the geodesy of other planets by measuring gravitational anomalies from subterranean features. Using AI measurements for detecting dark matter[14] and gravitational waves[15] have also been proposed.

The Aubin Lab at William & Mary aims to develop a novel microwave atom chip that supports broadband rf and microwave AC Zeeman potentials for spin-specific atom interferometry experiments.

II. AC ZEEMAN PHYSICS

The AC Zeeman (ACZ) effect is a resonant effect that describes the interaction between an atom with magnetic moment $\vec{\mu}$ and an oscillating magnetic field, $\vec{B}_{AC}$. This coupling leads to a shift in the atomic energy levels and can be described using dressed atom theory[16]. This ACZ energy shift is shown in Fig. 1 for a two-level system (i.e. the $|1,1\rangle \leftrightarrow |2,2\rangle$ 6.8 GHz hyperfine transition in ^{87}Rb). We see here that the eigenstates of the system, denoted by $|+\rangle$ and $|-\rangle$, experience either a solely positive ($|+\rangle$) or negative ($|-\rangle$) energy shift, independent of the frequency of the applied AC magnetic field. In the case of the $|+\rangle$ state, atoms in that state will feel a force pushing them towards regions of low magnetic field, i.e. it is a low-field seeking state. Conversely, the $|-\rangle$ state is a high-field seeking state.

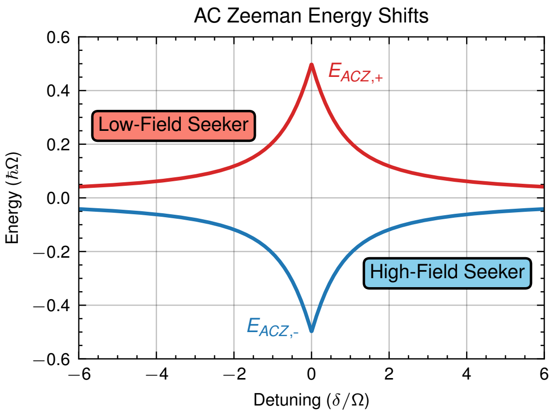

FIG. 1. AC Zeeman energy shifts for a two-level atom.

The Rabi frequency, Ω, which describes the strength of the coupling between the atom and AC field, can be written as[16]

$$\Omega = -\frac{\mu_B}{\hbar^2}\langle\downarrow|S_+B_- + S_-B_+ + 2S_zB_z|\uparrow\rangle, \qquad (1)$$

where μ_B is the Bohr magneton, $S_\pm = S_x \pm iS_y$ are the spin raising and lowering operators, $B_\pm = B_x \pm iB_y$ are circularly polarized magnetic fields, and $|\downarrow\rangle$ and $|\uparrow\rangle$ are the two states of our atom. From this equation we can see that to generate a trap for low-field seeking atoms in the $|+\rangle$ state using the ACZ potential we need to generate a minimum in the circularly polarized $B_\pm$ field.

Using the ACZ effect on an atom chip has multiple benefits over the traditional DC Zeeman chip traps:

- The ACZ effect is inherently **spin-specific**, allowing us to select favorable atomic states for atom interferometric sensing.
- We can **operate multiple traps simultaneously** on the chip, a key aspect for our atom interferometry schemes.
- ACZ traps can be **operated at arbitrary background magnetic field** allowing us to tune the field to suppress noise in the interferometer
- ACZ traps have been theoretically shown to **suppress potential roughness** effects[17], which we are currently exploring experimentally[18].

Our lab has demonstrated a trap using ACZ potentials on an atom chip[19] using ∼20 MHz rf currents to target intra-manifold transitions within a given ground-state hyperfine manifold of ^{87}Rb. This forms either a five (F=2) or three (F=1) level system, however, using 6.8 GHz inter-manifold transitions between hyperfine levels we can form an effective two-level system more conducive for interferometry. Since our lab's current atom chip is not designed to handle such high frequency currents, a new microwave atom chip must be developed. This chip must also be broadband out to at least 10 GHz to support ACZ potentials for multiple atomic species (Rb, K, Cs).

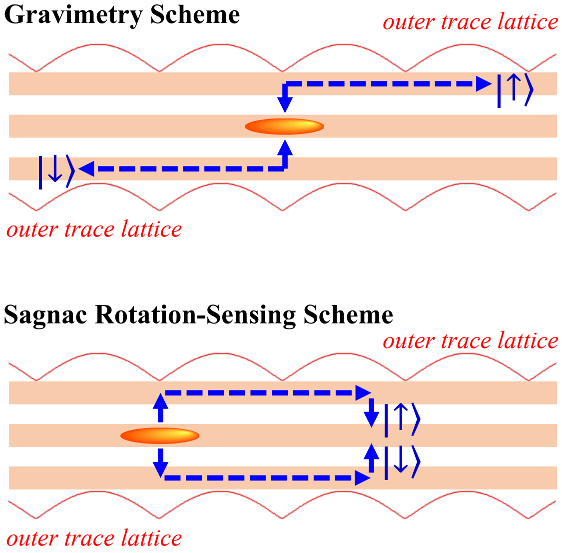

FIG. 2. Atom interferometry schemes for gravimetry (top) and rotation sensing (bottom) using spin-specific ACZ potentials on an atom chip. Figure taken from Miyahira et. al[16].

A. Atom Interferometry with AC Zeeman Traps

To make precision measurements of quantities such as gravitational gradients or inertial sensing using ultracold atoms on the chip, we use a technique known as atom interferometry. In our scheme using ACZ potentials, we can create an interferometer in the following way:

1. Prepare a sample of atoms in a coherent superposition of two spin states, $|\uparrow\rangle$ and $|\downarrow\rangle$, trapped in overlapping spin-specific potentials
2. Spatially separate the spin-specific potentials to microwave lattices (discussed later)
3. Translate the atoms axially along the outer microstrip traces
4. Recombine potentials to close the interferometer

This process can be visualized in Fig. 2 for gravimetry and Sagnac rotation-sensing schemes.

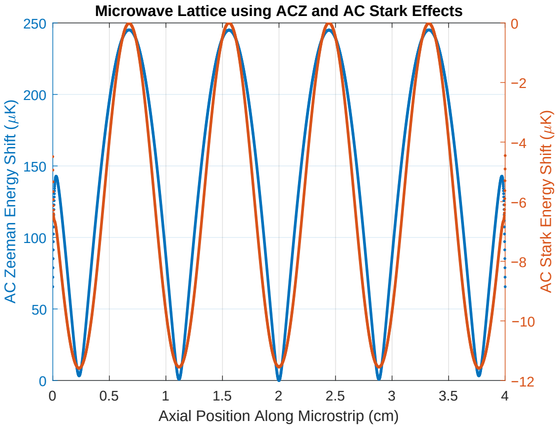

FIG. 3. Simulated microwave lattice for on-chip axial confinement and translation. The lattice can operate on either the AC Zeeman (blue) or AC Stark (orange) effect. For an aluminum nitride substrate the spacing between lattice minima is ∼0.9 cm. The simulation is done by sending counter-propagating 12.5 W signals at 6.8 GHz along a microstrip. The AC Zeeman potential operates on the $|2,2\rangle \leftrightarrow |1,1\rangle$ hyperfine transition in ^{87}Rb with a detuning of $2\pi\times$ 1 MHz. Figure taken from Miyahira et. al[16].

B. Microwave Lattice

In addition to the transverse (xy) confinement, we also need a scheme for trapping the atoms in the axial (z) direction. For this we plan to utilize a microwave lattice, as shown in Fig. 3[16]. The lattice is generated by sending counter-propagating microwaves along a single trace to form a standing wave that is stationary in time. This can operate either on the ACZ or AC Stark effect, depending on the applied frequency or desired lattice spacing. Fig. 3 shows a simulated lattice operating at 6.8 GHz on the $|1,1\rangle \leftrightarrow |2,2\rangle$ ^{87}Rb hyperfine transition, with a detuning of $2\pi\times1$ MHz. At this frequency the spacing between the lattice minima in AlN (ϵ_r=8.9) is ∼0.9 cm. The trapping potential is evaluated a distance of 100 μm above the surface of the chip and gives trapping frequencies of 30.1 and 2.8 Hz for the ACZ and AC Stark lattice, respectively.

In addition to axial confinement the lattice also allows us to translate the atoms axially for the atom interferometry schemes in Fig. 2. The position of the lattice minima is controlled by varying the phase difference of the signals generating the lattice. By transferring atoms to lattices on the outer chip microstrips we can then move each trap independently to achieve maximal arm separation for improved interferometer sensitivity.

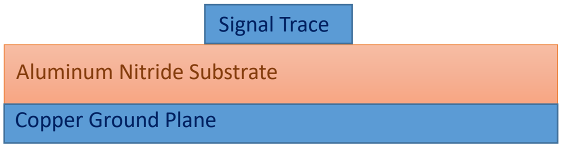

FIG. 4. Cross-section of a microstrip transmission line used on the broadband atom chip.

III. MICROWAVE ATOM CHIP

With the goal of being able to generate ACZ traps for multiple atomic species (i.e. K, Rb, Cs), we need an atom chip that can support a broad range of frequencies (DC-10 GHz or more). To achieve this broadband behaviour we utilize microstrip transmission lines as the building block of the atom chip. Fig. 4 shows a cross-section of this transmission line. This design features a signal trace separated from a copper ground plane by 50 μm of aluminum nitride (AlN), which has high thermal conductivity (170 W/m·K), advantageous for sending large amounts of current through the chip traces. The width of the signal trace is determined by the height of the substrate as well as its dielectric constant. For a typical AlN dielectric constant of $\epsilon_r = 8.9$, a trace width of 54 μm gives broadband 50 Ω impedance past 20 GHz[16].

Our atom chip design features is shown in Fig. 5. The chip features a 1 cm long "interferometry region" where the atom interferometry schemes in Fig. 2 will take place. In this region there are three parallel microstrips spaced 110 μm center-to-center. We can simulate the fields generated by this model using a high-frequency electromagnetic solver (FEKO by Altair) using the indicated parameters in the figure. Notably, the phase of the current in the central microstrip is 180° out-of-phase with the outer two. This simulation yields the trapping potential shown on the left in Fig. 5, which targets the $|2,2\rangle \leftrightarrow |1,1\rangle$ ^{87}Rb hyperfine transition with a detuning of $2\pi\times1$ MHz, producing a trap 109 μm above the chip surface with a trap depth of 15 μK and a transverse trapping frequency of $2\pi\times426$ Hz.

A. Microstrip Wedge Interface

One of the major engineering challenges we faced in the design of the microwave atom chip is finding a way to efficiently couple broadband rf and microwave signals onto the atom chip. Standard coaxial connectors can go down to a couple hundred microns in inner conductor diameter, however the microstrip traces comprising our atom chip are just

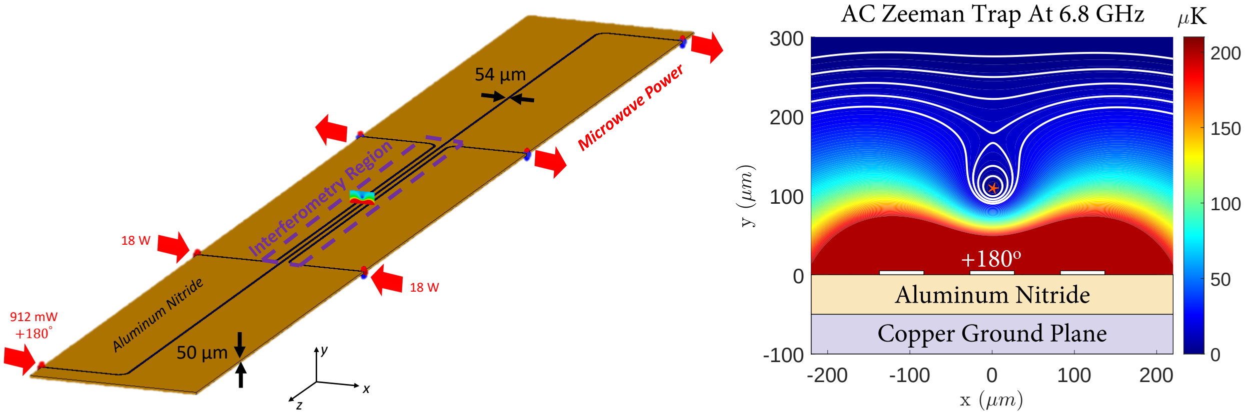

FIG. 5. Design and simulation of the new microwave atom chip. (Left) FEKO model of the atom chip, featuring three parallel microstrips in the central 1 cm long "interferometry region". The separation between the traces in this section is 110 μm center-to-center. The direction of the microwave power through the traces is indicated by the red arrows. A slice of the simulated trapping potential is shown at the center of the chip, however in reality this trap spans the whole "interferometry region". (Right) Simulated ACZ potential at 6.8 GHz using the parameters indicated on the left with a detuning of $2\pi\times1$ MHz on the $|2,2\rangle\leftrightarrow|1,1\rangle$ ^{87}Rb hyperfine transition. Here the current in the central microstrip is set 180° out-of-phase with the outer two microstrips, yielding an ACZ trap roughly 100 μm above the chip surface with a trap depth of 15 μK and a trap frequency of $2\pi\times426$ Hz. The white contour lines denote lines of constant temperature and are spaced every 5 μK.

54 μm wide. This difference in electromagnetic field mode size results in reflections at the interface of the coax and microstrip which could cause unwanted lattices on the atom chip. We simulated the effect of this size mismatch as shown in Fig. 6. In this model we looked at the coupling of various standard coaxial connector sizes (indicated by their inner conductor diameter) onto the atom chip microstrip. Naturally, we found that going down in size improves the reflection, however even with the smallest connector size we were only able to go out to about 7.5 GHz before the reflection got out of hand. To reach our goal of a broadband atom chip with the capability of operating in the 10-20 GHz range, we needed to devise a method of coupling the signals onto the chip while maintaining low reflection.

The method for broadband transmission onto the atom chip we are currently investigating is the tapered microstrip wedge interface, shown in Fig. 7. In this design, we begin by inserting a coaxial cable into the wide end of the wedge (W_1 in Fig. 7), which is designed to have 50 Ω impedance. The width of the microstrip is then tapered over a length L to the desired final microstrip width, W_2. For our atom chip this final width is ~50 μm. We are able to achieve broadband coupling between the coaxial input and our narrow atom chip traces because as the width of the wedge microstrip is narrowing, the substrate height is simultaneously decreasing, keeping the width-to-height ratio of the microstrip constant over the length of the wedge. Thus, the transmission line maintains a constant impedance as the signal

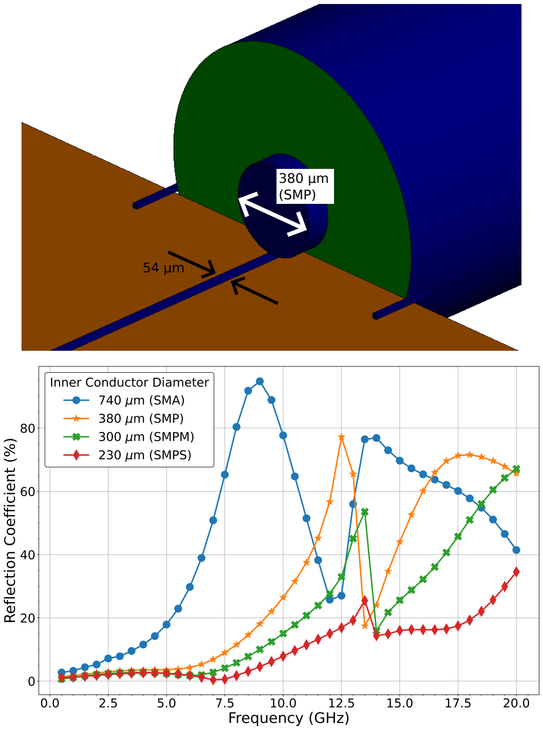

FIG. 6. FEKO simulation of a standard coaxial connector feeding a 54 μm wide atom chip microstrip trace. (Top) 3D CAD model of the simulation. (Bottom) Reflection coefficient versus frequency for a range of standard coaxial connector sizes, indicated by their inner conductor diameter. The outer conductor diameter of the coaxial connector was chosen to give a 50 Ω coax.

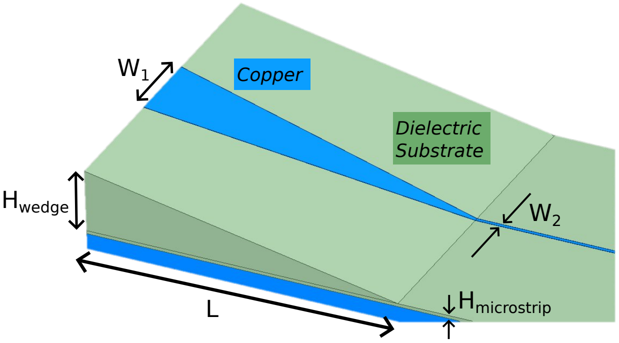

FIG. 7. Diagram of the tapered microstrip wedge interface. The ratio of substrate height to microstrip trace width is kept constant to maintain a 50 Ω impedance along the entire length of the wedge, L.

propagates down to the atom chip.

1. *Simulation*

To find out if the tapered wedge design yielded low reflection we began by simulating this interface using a popular high-frequency electromagnetic simulation software (Ansys HFSS). This software uses a finite element method (FEM) solver to solve Maxwell's equations giving the electromagnetic properties of the model.

Using the model in Fig. 7 we tailor the input width, W_1 to achieve the lowest broadband reflection coefficient for a given wedge height and dielectric constant.

We show results for a simulation of a tapered microstrip wedge interface in Fig. 8 for two different lengths of the wedge. In this model we use two wedges, one as an input and one as an output. The simulations show that we are able to achieve reflection coefficients below 4% out to 20 GHz for wedge lengths of 5 and 10 mm. The longer wedge lengths offer lower reflections as the transition between microstrip widths is less abrupt. However, we are primarily interested in shorter wedge lengths due to the size of our current ultra-high vacuum chamber apparatus[20].

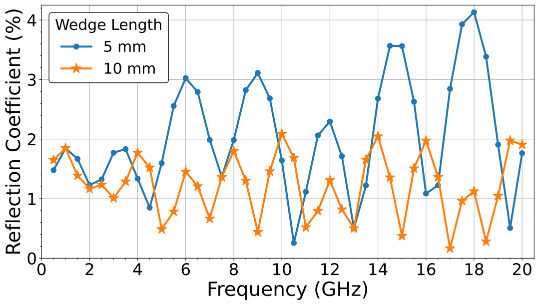

FIG. 8. HFSS simulation of the double-ended tapered microstrip wedge interface shown in Fig. 7. In this model, $W_1 = 1.1$ mm, $W_2 = 1.05$ mm, $W_1 = 54$ μm, $H_{\text{wedge}} = 1$ mm, and $H_{\text{microstrip}} = 50$ μm. Here the dielectric constant of the wedge and microstrip substrate is $\epsilon_r = 8.9$ (aluminum nitride).

TABLE I. Values of the heights and widths of the straight microstrip and microstrip wedge coupler. The dielectric constant of the substrate (RO4350b) is $\epsilon_r = 3.66$.

$H_{microstrip}$ (mm)	H_{wedge} (mm)	W_1 (mm)	W_2 (mm)
0.254	1.524	4.1	0.554
0.101	1.524	3.62	0.210

2. *Prototyping with RO4350b*

After seeing our simulations of the wedge interface display low reflection out to 20 GHz, we wanted to experiment with some larger-scale prototypes to verify the wedge design. Using Rogers 4350b (RO4350b, $\epsilon_r = 3.66$) as the substrate we designed and had made wedges of two sizes, listed in Table I. These parameters were simulated to give broadband 50 Ω impedance at each end of the wedge interface.

When manufacturing the wedge, it is impossible to achieve a perfect point at the end. Instead, you end up with a cliff with finite height. Simulations show that the wedge design is relatively robust to cliff sizes of roughly the final width, W_1, while maintaining low reflection coefficient. We measure this cliff size for the RO4350b wedges using a high-resolution optical microscope (Hirox). The average measured cliff size and standard deviation for both wedge sizes for 15 wedges is given in Table II. We observe cliff sizes below 50 μm for each size, well within the simulated tolerances.

Initial testing of the microstrip wedge interface us-

TABLE II. Values of the heights and widths of the straight microstrip and microstrip wedge coupler. The dielectric constant of the substrate (RO4350b) is 3.66. The data shows the average and standard deviation for 15 wedges of each size.

W_2 (mm)	Average Cliff Size (μm)	Stdev (μm)
0.554	47.8	11.3
0.210	40.3	7.3

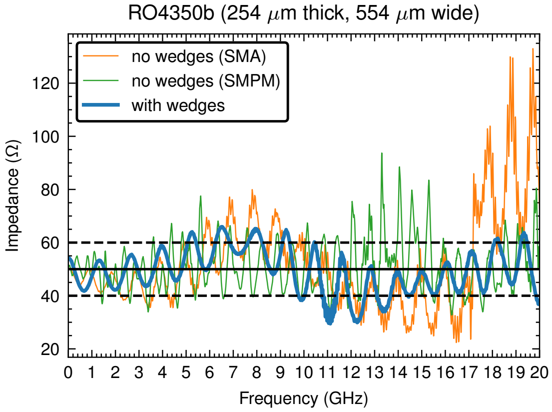

FIG. 9. Initial test comparing the use of the microstrip wedge interface (blue data) versus traditional coaxial connectors (orange and green data). The wedge paramters in this design are found in the first row of Table I. The black lines indicate 50 Ω (solid) and ±10 Ω (dashed) impedance.

ing the RO4350b substrate is shown in Fig. 9. We compare the result of using the tapered wedge interface versus a standard SMA and SMPM edge launch connector. Here the wedge input is fed by a SMA connector. We observe very promising results from this initial test, as the use of wedges yields smaller impedance spikes and a more stable impedance out to 20 GHz. Additionally, we've seen that the wedge can be tuned to the specific SMA connector used to feed microwaves to the circuit by shaving the end to match the size of the EM field mode of the connector, giving smaller impedance fluctuations more centered on 50 Ω.

B. Material Characterization

In order to achieve broadband 50 Ω microstrip transmission lines on the atom chip, the dielectric constant of the substrate must be well known. In our case, this will set the width of the microstrip. To determine the dielectric constant of the material, we have designed and simulated a microstrip resonator circuit, shown in Fig. 10. In this design we create an impedance mismatch in the microstrip by abruptly changing its width to a much wider trace (while the substrate height remains constant). This creates a cavity in the wide central region that allows signals to pass through only at specific frequencies, or resonances. The spacing between these resonant frequencies is related to the dielectric constant of the material, and can provide us with an accurate measurement of ϵ_r for our AlN material. Additionally, we can put an upper limit on the loss tangent for the material, tan(δ), another key microwave characteristic, and is related to the width of the resonances.

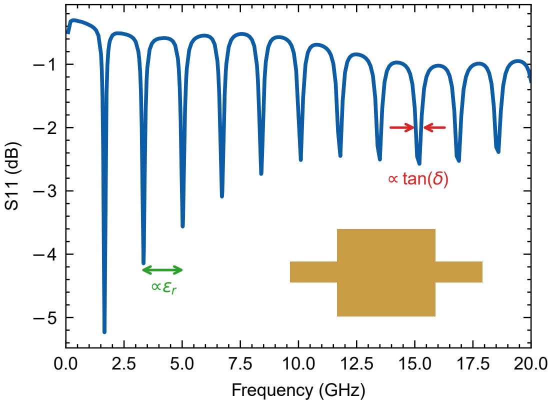

FIG. 10. SONNET simulation of the microstrip resonator circuit (shown in bottom right corner) for determining the dielectric constant and loss tangent of the aluminum nitride substrate. The design of the resonator is shown in the lower right corner. The spacing between resonances in the reflection coefficient S_{11} is proportional to the dielectric constant ϵ_r while the width of the resonance will yield an upper bound on the loss tangent, tan(δ).

C. Atom Chip Manufacturing

Before being able to do any photo-lithography on the atom chip, the substrate must first be carefully prepared. To ensure minimal impedance fluctuations of the atom chip microstrips the substrate must be made very flat. Any large bumps seen by the microstrips will cause the impedance to change resulting in potentially large reflections. Thus, the copper onto which the AlN substrate will be deposited must itself be made very flat. Additionally, it must be rigid enough to not deform during the deposition process while still being thin enough to quickly dissipate eddy currents from fast turn-offs of DC current on the chip wires.

1. Diamond Turning

To achieve a flat surface of the Cu-AlN-Cu sandwiches, we had them diamond turned. This process uses a diamond machining bit to remove a small amount of material from the surface of the copper leaving behind a flat, mirror-like surface. To characterize the flatness of the diamond turned surface we looked at some of the Cu-AlN-Cu samples using

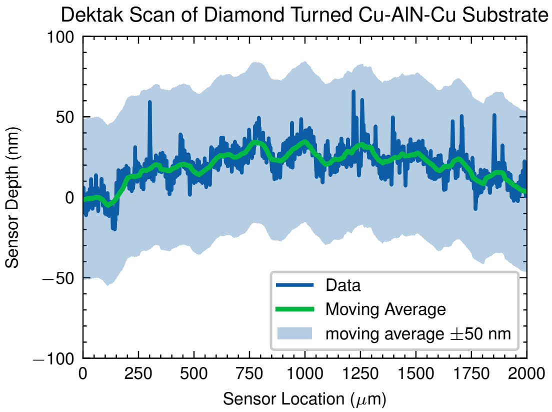

FIG. 11. Dektak scan of a diamond turned Cu-AlN-Cu sandwich prior to deposition of AlN onto the copper surface. A moving average (green line) is placed on the data (dark blue line) for better visualization, along with a ±50 nm shaded region. The surface roughness observed here is on the order of a few tens of nm, a few orders of magnitude smaller than the intended deposition thickness of 50 μm.

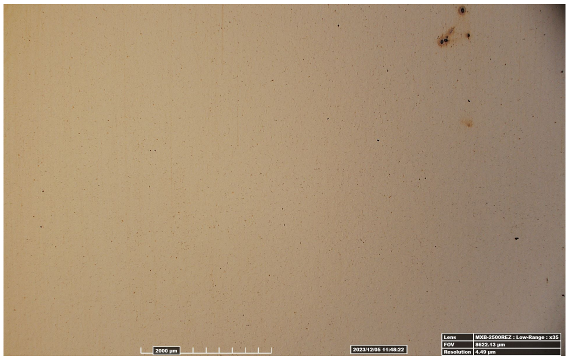

FIG. 12. Hirox microscope image of the Cu-AlN-Cu sample surface. This is the same sample as in Fig. 11.

a surface profiler (Bruker Dektak XT). This device drags a stylus across the surface of the material and tracks changes in sensor depth with angstrom level sensitivity. Fig. 11 shows a 2 mm Dektak scan of one of the Cu-AlN-Cu diamond turned samples. After diamond turning we are able to see surface roughness under 50 nm (0.05 μm), sufficient for deposition and micro-fabrication. This data is consistent across different locations of the same sample and with other samples we tested on the Dektak. For reference, prior to diamond turning we observed surface roughness on the order of 1-2 μm. Roughness of this size should impact the impedance of the microstrip lines on the order of ∼0.1%.

D. Phase Controlled Microwave Source

One of the key experimental parameters for operating the ACZ chip trap is being able to precisely control and manipulate the relative phase and frequency of the microwaves in neighboring microstrip traces. This phase difference controls the trap position, polarization, and frequency, for example. Additionally, for axial translations along the trace via a microwave lattice controlling the relative phase is crucial.

We have designed and constructed multiple 6.8 GHz microwave sources with low phase-noise and digital phase control between channels based on IQ modulation. In this scheme, an ultra-low phase noise microwave source at 3.2 GHz (Holzworth 4001b) is mixed with a high-quality rf source at 200 MHz (WeiserLabs Flex-DDS) to produce a signal at 3.4 GHz. After sufficient filtering we can produce an essentially pure 3.4 GHz signal which can be doubled to 6.8 GHz (^{87}Rb ground state hyperfine splitting). The IQ mixing process allows us to digitally control the relative phase between sources, and we've observed a ±50 MHz scan range off of 6.8 GHz, which should be sufficient for our experimental applications.

IV. ROUGHNESS SUPPRESSION

One of the proposed benefits of using ACZ trapping potentials on a chip is the suppression of potential roughness. This effect originates from manufacturing defects in the atom chip wires that can manifest themselves in the trapping potential for the ultracold atoms. These manufacturing defects can be non-uniform wire conductivity or indents on the edges of the wire, for example. Any such defect will cause the current in the wire to deviate from an ideal straight line. This results in regions of local axial confinement that can fragment the atom cloud. These effects magnify as the atoms are moved closer to the chip surface and can negatively effect atom interferometry experiments. Previous theoretical work has been done to show suppression factors of $\sim 10^4$ using an ACZ trap over the traditional DC Zeeman trapping schemes[17]. We are currently working on an experimental effort to explore this roughness suppression using our current atom chip. Additional suppression should manifest at higher frequencies (i.e. 6.8 GHz on the microwave atom chip) due to the AC skin effect.

We can extract a trapping potential from absorption images of the atoms through the equation

$$U(z) = -k_B T \ln(n(z)), \tag{2}$$

where k_B is Boltzmann's constant, T is the temperature of the atoms, and $n(z)$ is the atom number density. Preliminary results of these experiments are shown in Fig. 13. Here, we trap ultracold atoms (1-2 μK) in identical two-wire DC and rf AC Zeeman chip traps. Identical here refers to the traps being at the same location and having the same transverse trapping frequency, in addition to using the same chip wires for performing the trapping. Though these are still initial results we already observe qualitative evidence of roughness suppression in the rf ACZ trap. In the DC trap there is clear fragmentation of the atom cloud due to roughness, where we get three distinct local potential wells in addition to the long-ranging harmonic potential. These roughness bumps are suppressed in the rf ACZ trap, giving a noticeably smoother potential without any fragmentation of the atom cloud. We not that the bump observed at ~1,000 μm in both traps is suppressed by about a factor of 4 in the ACZ trap, though more recent efforts to refine the experiment show that it might be even more.

V. CONCLUSION

We have presented work towards the development of a novel broadband microwave atom chip for spin-specific trapped atom interferometery and quantum sensing. The design of the chip features parallel microstrip transmission lines for generating the transverse trapping potentials. Axial confinement and translation is provided via a microwave lattice based on the ACZ or AC Stark effect. To efficiently couple broadband rf and microwave signals onto the atom chip we have developed a tapered microstrip wedge interface which has shown operation in both simulation and initial prototype testing. We have begun the manufacturing of the atom chip by diamond turning the copper surfaces on which a thin layer of aluminum nitride will be deposited. Once the deposition is complete we can fabricate a microstrip resonator to determine the dielectric constant and loss tangent of the material.

ACKNOWLEDGMENTS

WHM is supported by the Virginia Space Grant Consortium (VSGC), NSF Grant #2̃308767, DTRA #H̃DTRA1-19-1-0027, with partial funding from a VMEC Seed Grant from ARL. We would also like to acknowledge collaborations with Professor Vitaly Avrutin (VCU), David Pate (VCU), and Trevor Tingle (W&M) as well as with the teams at Nitride Global, LLC. and Kaddco Ceramics. Additionally, we would like to thank Will Henninger for his machining expertise and Doug Berringer (W&M ARC Lab) for his help with material characterization.

---

[1] M. H. Anderson, J. R. Ensher, M. R. Matthews, C. E. Wieman, and E. A. Cornell, Observation of bose-einstein condensation in a dilute atomic vapor, Science **269**, 198 (1995).

[2] S. M. Dickerson, J. M. Hogan, A. Sugarbaker, D. M. Johnson, and M. A. Kasevich, Multiaxis inertial sensing with long-time point source atom interferometry, Physical review letters **111**, 083001 (2013).

[3] M. Keil, O. Amit, S. Zhou, D. Groswasser, Y. Japha, and R. Folman, Fifteen years of cold matter on the atom chip: promise, realizations, and prospects, Journal of modern optics **63**, 1840 (2016).

[4] D. C. Aveline, J. R. Williams, E. R. Elliott, C. Dutenhoffer, J. R. Kellogg, J. M. Kohel, N. E. Lay, K. Oudrhiri, R. F. Shotwell, N. Yu, *et al.*, Observation of bose–einstein condensates in an earth-orbiting research lab, Nature **582**, 193 (2020).

[5] E. R. Elliott, D. C. Aveline, N. P. Bigelow, P. Boegel, S. Botsi, E. Charron, J. P. d'Incao, P. Engels, T. Estrampes, N. Gaaloul, *et al.*, Quantum gas mixtures and dual-species atom interferometry in space, Nature **623**, 502 (2023).

[6] R. Carollo, D. Aveline, B. Rhyno, S. Vishveshwara, C. Lannert, J. Murphree, E. Elliott, J. Williams, R. Thompson, and N. Lundblad, Observation of ultracold atomic bubbles in orbital microgravity (2021), arXiv preprint arXiv:2108.05880.

[7] J. R. Williams, C. A. Sackett, H. Ahlers, D. C. Aveline, P. Boegel, S. Botsi, E. Charron, E. R. Elliott, N. Gaaloul, E. Giese, *et al.*, Interferometry of atomic matter waves in the cold atom lab onboard the international space station, arXiv preprint arXiv:2402.14685 (2024).

[8] K. Frye, S. Abend, W. Bartosch, A. Bawamia, D. Becker, H. Blume, C. Braxmaier, S.-W. Chiow, M. A. Efremov, W. Ertmer, *et al.*, The bose-einstein condensate and cold atom laboratory, EPJ Quantum Technology **8**, 1 (2021).

[9] R. Thompson, D. Aveline, S. Chiow, E. Elliott, J. Kellogg, J. m Kohel, M. Sbroscia, L. Phillips, C. Schneider, J. Williams, *et al.*, Exploring the quantum world with a third generation ultra-cold atom facility, Quantum Science and Technology **8**, 014007 (2022).

[10] F. Webb, F. Fletchtner, F. Landerer, P. Morton, M. Watkins, H. Save, C. Dahle, S. Bettadpur, R. Gaston, and M. Gross, Gravity recovery and climate experiment follow-on mission, (2019).

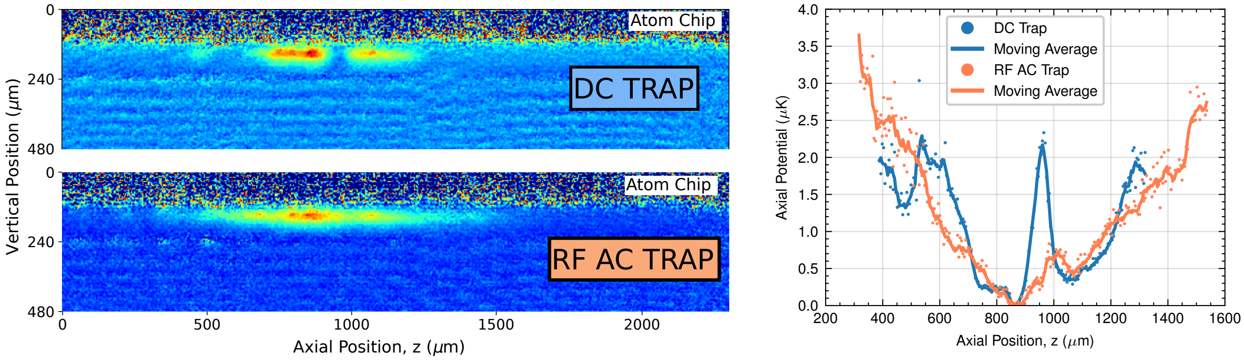

FIG. 13. Preliminary results demonstrating potential roughness suppression in an ACZ chip trap. (Right) Absorption images of atoms trapped in the DC (top) and AC (bottom) Zeeman chip trap. These images are averaged over 75 shots using a 1 ms time-of-flight before imaging. (Right) Extracted axial trapping potentials from the absorption images using Eqn. 2. The temperatures in each trap are 0.99 μK and 1.68 μK for the DC and AC traps, respectively.

[11] R. Kaltenbaek, A. Acin, L. Bacsardi, P. Bianco, P. Bouyer, E. Diamanti, C. Marquardt, Y. Omar, V. Pruneri, E. Rasel, *et al.*, Quantum technologies in space, Experimental Astronomy **51**, 1677 (2021).

[12] B. Barrett, A. Bertoldi, and P. Bouyer, Inertial quantum sensors using light and matter, Physica Scripta **91**, 053006 (2016).

[13] I. Dutta, D. Savoie, B. Fang, B. Venon, C. G. Alzar, R. Geiger, and A. Landragin, Continuous cold-atom inertial sensor with 1 nrad/sec rotation stability, Physical review letters **116**, 183003 (2016).

[14] A. Arvanitaki, P. W. Graham, J. M. Hogan, S. Rajendran, and K. Van Tilburg, Search for light scalar dark matter with atomic gravitational wave detectors, Physical Review D **97**, 075020 (2018).

[15] J. M. Hogan and M. A. Kasevich, Atom-interferometric gravitational-wave detection using heterodyne laser links, Physical Review A **94**, 033632 (2016).

[16] W. Miyahira, A. P. Rotunno, S. Du, and S. Aubin, Microwave atom chip design, Atoms **9**, 54 (2021).

[17] S. Du, A. Ziltz, W. Miyahira, and S. Aubin, Suppression of potential roughness in atom-chip ac zeeman traps, Physical Review A **105**, 053127 (2022).

[18] W. Miyahira and S. Aubin, Potential roughness suppression in a rf ac zeeman atom chip trap, in *Quantum Sensing, Imaging, and Precision Metrology II*, Vol. 12912 (SPIE, 2024) pp. 247–251.

[19] A. Rotunno, *Radiofrequency AC Zeeman Trapping for Neutral Atoms*, Ph.D. thesis, College of William & Mary (2021).

[20] M. Ivory, A. Ziltz, C. Fancher, A. Pyle, A. Sensharma, B. Chase, J. Field, A. Garcia, D. Jervis, and S. Aubin, Atom chip apparatus for experiments with ultracold rubidium and potassium gases, Review of Scientific Instruments **85**, 043102 (2014).